

1 Revision2 - 12/31/2012

2 **Kangite, (Sc,Ti,Al,Zr,Mg,Ca, \square)₂O₃, a new ultrarefractory scandia mineral**
3 **from the Allende meteorite: Synchrotron micro-Laue diffraction and**
4 **electron backscatter diffraction**

5 Chi Ma^{1*}, Oliver Tschauner^{1,2}, John R. Beckett¹, George R. Rossman¹, Wenjun Liu³
6

7 ¹Division of Geological and Planetary Sciences, California Institute of Technology, Pasadena, CA
8 91125, USA; ²High Pressure Science and Engineering Center and Department of Geoscience,
9 University of Nevada, Las Vegas, NV 89154, USA; ³Advanced Photon Source, Argonne
10 National Laboratory, Argonne, IL 60439, USA.

11

12

13

ABSTRACT

14

15

16

17

18

19

20

21

22

23

24

25

26

27

28

29

30

Kangite (IMA 2011-092), (Sc,Ti,Al,Zr,Mg,Ca, \square)₂O₃, is a new scandia mineral, occurring as micrometer-sized crystals with REE-rich perovskite and spinel in a davisite-dominant ultrarefractory inclusion from the Allende CV3 carbonaceous chondrite. The phase was characterized by SEM, EBSD, synchrotron micro-Laue diffraction, micro-Raman and EPMA. The mean chemical composition of the type kangite is (wt%) TiO₂ 36.6, Sc₂O₃ 26.4, ZrO₂ 11.3, Al₂O₃ 7.0, Y₂O₃ 5.4, CaO 3.9, MgO 3.14, Dy₂O₃ 1.8, SiO₂ 1.7, V₂O₃ 1.31, Er₂O₃ 0.92, FeO 0.8, Gd₂O₃ 0.60, Ho₂O₃ 0.40, Tb₂O₃ 0.18, Cr₂O₃ 0.09, ThO₂ 0.04, O -0.3, sum 101.28 with a corrected empirical formula calculated on the basis of 3 O atoms of [(Sc_{0.54}Al_{0.16}Y_{0.07}V_{0.03}Gd_{0.01}Dy_{0.01}Er_{0.01})³⁺_{Σ0.83}(Ti_{0.66}Zr_{0.13})⁴⁺_{Σ0.79}(Mg_{0.11}Ca_{0.06}Fe_{0.02})²⁺_{Σ0.19} \square _{0.19}]_{Σ2.00}O₃. Synchrotron micro-Laue diffraction (i.e., an energy scan by a high flux X-ray monochromatic beam) on one type domain at submicrometer resolution revealed that kangite has a cation deficient *Ia* $\bar{3}$ bixbyite-type cubic structure. The cell parameters are *a* = 9.842(1) Å, *V* = 953.3(1) Å³, *Z* = 16, which leads to a calculated density of 3.879 g/cm³. Kangite is a new ultrarefractory mineral, likely originating through low temperature

31 oxidation of a Sc-, Ti³⁺-enriched high temperature condensate oxide dating to the
32 birth of the solar system.

33

34 **Keywords:** Kangite, (Sc,Ti,Al,Zr,Mg,Ca,□)₂O₃, new ultrarefractory mineral, scandia,
35 Allende meteorite, CV3 carbonaceous chondrite, synchrotron micro-Laue diffraction, EBSD.
36 *E-mail: chi@gps.caltech.edu

37

38 INTRODUCTION

39 During a nanomineralogy investigation of a previously described inclusion, ACM-3,
40 in the Allende meteorite (Ma and Rossman 2009b), a new ultrarefractory Sc-, Ti-rich mineral
41 (Sc,Ti,Al,Zr,Mg,Ca,□)₂O₃, named “kangite,” was discovered. Electron probe microanalysis
42 (EPMA), high-resolution scanning electron microscope (SEM), electron backscatter
43 diffraction (EBSD), synchrotron micro-Laue diffraction with subsequent energy scans, and
44 microRaman analyses were used to determine its composition, physical properties, and
45 structure and to characterize associated phases. Synthetic Sc₂O₃ is well-known but synthetic
46 (Sc,Ti,Al,Zr,Mg,Ca,□)₂O₃ is unknown. Kangite is a new mineral species and a phase new to
47 meteoritics. In this paper, we describe the first occurrence of kangite in nature, as a new
48 ultrarefractory oxide, among the oldest solid materials in the solar system.

49

50 MINERAL NAME AND TYPE MATERIAL

51 The mineral and the mineral name (kangite) have been approved by the Commission
52 on New Minerals, Nomenclature and Classification (CNMNC) of the International
53 Mineralogical Association (IMA 2011-092). The name is derived from “kang”, the Chinese
54 word for the element scandium. Holotype material has been deposited under catalog USNM
55 7555 in the Smithsonian Institution’s National Museum of Natural History, Washington DC,
56 USA. Section USNM 7555 also contains type davisite (IMA 2008-030; Ma and Rossman
57 2009b).

58

59 OCCURRENCE

60 The Allende meteorite fell in and near Pueblito de Allende, Chihuahua, Mexico on
61 February 8, 1969 (Clarke et al. 1971). This CV3 carbonaceous chondrite is probably the most
62 highly studied meteorite and the results of these studies have greatly influenced current

63 thinking about processes, timing, and chemistry in the primitive solar nebula and in small
64 planetary bodies. The mineral kangite was found within one irregular ultrarefractory
65 inclusion, ACM-3, in one polished section (USNM 7555), prepared from a ~1 cm diameter
66 Allende fragment (Caltech Meteorite Collection No. Allende12A). ACM-3 is about 130 μm
67 in diameter in the section plane and is surrounded by a matrix of mostly fine-grained olivine
68 and troilite. Kangite occurs interstitially, along with perovskite and spinel, within an
69 aggregate of the type davisite crystals (Figs. 1-2). All four kangite grains are in contact with
70 davisite and two are also in contact with perovskite. One was observed in contact with
71 spinel.

72

73 **APPEARANCE, PHYSICAL, AND OPTICAL PROPERTIES**

74 Kangite occurs as four irregular to subhedral grains, 1 to 4 μm in size, which
75 constitute the type material (Fig. 2). In the optically thick section (150 μm in thickness),
76 kangite is opaque. Color, streak, luster, hardness, tenacity, cleavage, fracture, density and
77 refractive index were not determined because of the small grain size. Given the large extent
78 of solid solution in the natural material and its cation deficient stoichiometry, it is unlikely
79 that these properties are close to those of synthetic Sc_2O_3 . The density, calculated from its
80 crystal structure and the empirical formula, is 3.879 g/cm^3 , which is similar to those of Sc_2O_3
81 (3.86) and panguite (3.75), but lower than those of TiO_2 (4.59) and Ti_2O_3 (4.23). Kangite is
82 not cathodoluminescent under the electron beam in an SEM and we observed no crystal
83 forms or twinning. Visible light fluorescence can be excited by light of 514.5 nm; we did not
84 check for fluorescence using alternative wavelengths.

85

86 **CHEMICAL COMPOSITION**

87 Chemical analyses of kangite (on the two leftmost grains in Fig. 2) and associated
88 minerals were carried out using a JEOL 8200 electron microprobe (WDS: 15 kV; 5 nA and
89 25 nA; beam in focused mode) interfaced with the Probe for EPMA program from Probe
90 Software, Inc. Possible interferences on peak position and background position were checked
91 and corrected for all measured elements based on WDS scans and using the Probe for EPMA;
92 on-peak interferences of $\text{TiK}\alpha$ by Sc, $\text{VK}\alpha$ by Ti and Y, $\text{CrK}\alpha$ by V, $\text{ErL}\alpha$ by Tb, $\text{HoL}\alpha$ by
93 Gd, $\text{LaL}\alpha$ by Nd, $\text{CeL}\alpha$ by Ti and V, and $\text{NdL}\alpha$ by Ce were corrected. Standards for the
94 analysis were TiO_2 ($\text{TiK}\alpha$, $\text{OK}\alpha$), ScPO_4 ($\text{ScK}\alpha$), zircon ($\text{ZrL}\alpha$), anorthite ($\text{CaK}\alpha$, $\text{AlK}\alpha$,
95 $\text{SiK}\alpha$), YPO_4 ($\text{YL}\alpha$), forsterite ($\text{MgK}\alpha$), fayalite ($\text{FeK}\alpha$), DyPO_4 ($\text{DyL}\alpha$), ErPO_4 ($\text{ErL}\alpha$),
96 GdPO_4 ($\text{GdL}\alpha$), TbPO_4 ($\text{TbL}\alpha$), HoPO_4 ($\text{HoL}\alpha$), ThO_2 ($\text{ThM}\alpha$), V_2O_3 ($\text{VK}\alpha$), Cr_2O_3 ($\text{CrK}\alpha$),

97 LaPO₄ (LaLα), CePO₄ (CeLα), NdPO₄ (NdLα), SmPO₄ (SmLα), and YbPO₄ (YbLα).
98 Quantitative elemental microanalyses were processed with the CITZAF correction procedure
99 (Armstrong 1995) and analytical results are given in Table 1. No other element with an
100 atomic number exceeding 4 was detected by WDS scans at 15 kV, 25 nA and 300 nA. In
101 particular, none of the light rare earth elements (LREE) nor Yb was detected in kangite or in
102 associated perovskite and davisite; detection limits for these elements at 99% confidence
103 were 0.03 wt% for Sm and 0.04 wt% for La, Ce, Nd, and Yb. On-peak WDS X-ray mapping
104 of Sc, Zr, Y, and Dy in ACM-3 (Fig. 3) was carried out at 15 kV and 100 nA, counting for
105 500 ms per pixel. The 250 x 320 pixel maps were collected using a 0.5 μm step size and
106 without a background correction.

107 The empirical formula of type kangite as analyzed by EPMA, based on three oxygens,
108 is [(Sc_{0.53}Al_{0.19}Y_{0.07}V_{0.02}Gd_{0.01}Dy_{0.01}Er_{0.01})³⁺_{Σ0.84}(Ti_{0.63}Zr_{0.13}Si_{0.04})⁴⁺_{Σ0.80}
109 (Mg_{0.11}Ca_{0.10}Fe_{0.02})²⁺_{Σ0.23}□_{0.13}]_{Σ2.00}O₃, where the oxidation states of Ti, V, and Fe are
110 assumed to be 4+, 3+, and 2+, respectively. Oxygen analyses by EPMA (at 15kV and 25 nA,
111 using LDE1 crystal for OKα measurement and synthetic TiO₂ as standard) in both kangite
112 and perovskite support Ti⁴⁺ (*versus* Ti³⁺) in kangite, as shown in Table 1 where leftover O in
113 kangite (also perovskite) is roughly one standard deviation of the measured oxygen content
114 when all Ti is assigned to 4+. If all Ti is assumed to be 3+, then leftover oxygen in kangite is
115 3.4 wt% (i.e., an order of magnitude higher than the analytical error). We cannot reject the
116 possibility that minor Ti is trivalent as 8 % of the Ti in the kangite analysis in Table 1 would
117 be Ti³⁺ if the measured oxygen content is used to calculate Ti³⁺/Ti⁴⁺ (contamination from
118 nearby davisite, which is Ti³⁺-enriched (Ma and Rossman 2009b), does not significantly
119 affect this calculation). Nevertheless, EPMA analyses clearly indicate that Ti in kangite is
120 dominantly 4+. We cannot be certain of the valence for Fe or V because the concentrations
121 are too low. Some of the Fe in kangite could be ferric as alloys in Allende refractory
122 inclusions were often oxidized to magnetite during low temperature metasomatism (Blum et
123 al. 1989) and some of the V could be divalent as roughly half of the V in clinopyroxene and
124 spinel from Ca-, Al-rich inclusions from Allende is V²⁺ (Simon et al. 2007; Paque et al.
125 2010). Changing the assigned valences for Fe and/or V has a negligible effect on the inferred
126 crystallographic properties and no effect on the nomenclature of kangite or our conclusions
127 regarding origin. The apparent Si content in kangite is likely derived from the surrounding
128 davisite, because of the small grain size. If all Si and associated cations in the form of
129 surrounding davisite are removed, kangite shows a formula of

130 $[(\text{Sc}_{0.54}\text{Al}_{0.16}\text{Y}_{0.07}\text{V}_{0.03}\text{Gd}_{0.01}\text{Dy}_{0.01}\text{Er}_{0.01})^{3+}_{\Sigma 0.83}(\text{Ti}_{0.66}\text{Zr}_{0.13})^{4+}_{\Sigma 0.79}(\text{Mg}_{0.11}\text{Ca}_{0.06}\text{Fe}_{0.02})^{2+}_{\Sigma 0.19}\square_{0.19}$
131 $]\Sigma_{2.00}\text{O}_3$. Kangite is much more Ti- and Sc-rich than previously reported zirconias and is
132 more Sc-rich than panguite (Fig. 4). Based on EPMA, kangite exhibits an ultrarefractory rare
133 earth element (REE) pattern in which most of the heavy REE (HREE) are greatly enriched
134 relative to the LREE and Yb is depleted relative to the other HREE (concentrations of La, Ce,
135 Nd, Sm, and Yb are all below EPMA detection limits, 0.03-0.04 wt%) (Fig. 5). The general
136 formula for kangite is $(\text{Sc,Ti,Al,Zr,Mg,Ca},\square)_2\text{O}_3$, or $(\text{Sc,Ti,Al,Zr,Mg,Ca})_{1.8}\text{O}_3$, where Sc^{3+} is
137 the dominant trivalent component and the trivalent cations are dominant in the cation sites
138 without indications for cation ordering. The IMA-approved dominant-valency rule (Hatert
139 and Burke 2008) is applied here to designate this oxide as a new Sc mineral. The ideal end-
140 member formula is Sc_2O_3 .

141 Kangite occurs within an aggregate of 2-12 μm diameter crystals of davisite, whose
142 Sc_2O_3 content ranges from as high as 17.66 wt% in portions of the inclusion near the spray of
143 kangite and perovskite crystals, to as low as 8.05 wt% near the inclusion-matrix boundary
144 and in the two lower lobes of the inclusion (the lobe containing the "spinel" label in Fig. 1
145 and the smaller lobe above and to the left of it; see also the Sc X-ray map in Fig. 3). Davisite
146 in the central region surrounding kangite and perovskite has a mean composition of
147 $\text{Ca}_{0.98}(\text{Sc}_{0.52}\text{Ti}^{3+}_{0.17}\text{Mg}_{0.14}\text{Ti}^{4+}_{0.09}\text{Zr}_{0.04}\text{V}^{3+}_{0.02}\text{Y}_{0.02}\text{Al}_{0.01}\text{Fe}^{2+}_{0.01})(\text{Si}_{1.00}\text{Al}_{1.00})\text{O}_6$, where
148 partitioning of Ti^{3+} and Ti^{4+} is based on a stoichiometric formula unit containing 4.00 cations
149 and 6 oxygens. High Sc davisite is HREE enriched (LREE are below detection limits) but
150 concentrations are a factor of several to an order of magnitude lower than in perovskite and
151 kangite. Low Sc davisite is also lower in Zr and HREE than high Sc crystals, showing an
152 average formula of $\text{Ca}_{0.98}(\text{Sc}_{0.30}\text{Ti}^{3+}_{0.19}\text{Mg}_{0.31}\text{Ti}^{4+}_{0.08}$
153 $\text{Al}_{0.07}\text{Zr}_{0.02}\text{V}^{3+}_{0.02}\text{Y}_{0.01}\text{Fe}^{2+}_{0.01})(\text{Si}_{1.20}\text{Al}_{0.80})\text{O}_6$. If kangite and nearby davisite equilibrated with
154 each other (although this may not have been the case, as discussed below), the compositions
155 (Table 1; Fig. 3) imply that Zr, V, Y and the REE are strongly partitioned into kangite
156 relative to davisite and Ca and, to a lesser extent, Al in davisite relative to kangite; the Ti
157 oxide panguite displays similar partitioning relationships with associated davisite (Ma et al.
158 2012). Note that about two-thirds of the Ti in davisite is inferred to be trivalent while
159 coexisting kangite contains little if any Ti^{3+} . One possible interpretation of this observation is
160 that kangite strongly preferred Ti^{4+} and discriminated against Ti^{3+} relative to davisite.
161 However, we argue below that kangite is the low temperature oxidation product of a high

162 temperature Ti³⁺-rich phase. Relative concentrations of cations were not significantly
163 affected but the additional oxygen was accommodated through the transformation of Ti³⁺ to
164 Ti⁴⁺.

165 Perovskite in the kangite type example (Figs. 1-2) is Y-rich (Table 1) but Zr-poor
166 (~0.1 wt %), with a formula of (Ca_{0.82}Y_{0.08}Dy_{0.03}Gd_{0.02}Sc_{0.02}Fe_{0.01}Er_{0.01}V_{0.01})(Ti_{0.94}Al_{0.02})O₃.
167 As in kangite, the perovskite is HREE enriched with concentrations of LREE below EPMA
168 detection limits (Table 1; Fig. 5). Perovskite with similar REE abundances described by
169 Weber and Bischoff (1994) is relatively Zr-rich (ZrO₂ 4 wt%). Associated spinel (Fig. 2) is
170 Fe-rich (FeO 11.22 wt%) with 0.42 wt% TiO₂, 0.38 wt% V₂O₃, and 0.30 wt% Cr₂O₃ (Table
171 1), showing a formula of (Mg_{0.79}Fe_{0.24})(Al_{1.95}Ti_{0.01}V_{0.01}Cr_{0.01})O₄. We note that stoichiometry
172 considerations require Fe²⁺>>Fe³⁺ for this phase (i.e., the spinel is hercynitic). The valence
173 state of Ti in the spinel, which can be either Ti³⁺- or Ti⁴⁺-enriched, at least in type B1
174 inclusions (Paque et al. 2010), is unknown. Overall, V-Ti-Cr concentrations are higher than
175 for most reported spinels from meteoritic inclusions in carbonaceous chondrites (e.g.,
176 Connolly and Burnett 1999; Connolly et al. 2003) but they are not diagnostic because
177 similarly enriched compositions, although rare, are occasionally encountered in wide variety
178 of inclusion types including fine-grained (Krot et al. 2004), compact type A (Srinivasan et al.
179 2000), fluffy type A (Allen et al. 1978), and type B1 inclusions (Wark and Lovering 1982; El
180 Goresy et al. 1985; Armstrong et al. 1987).

181

182 CRYSTALLOGRAPHY

183

184 *EBSD AND SYNCHROTRON MICRO-LAUE DIFFRACTION*

185 EBSD analyses at a submicrometer scale were performed on the vibration-polished
186 section using methods described in Ma and Rossman (2008a, 2009a). An HKL (now Oxford)
187 EBSD system on a Zeiss 1550VP scanning electron microscope was used for these
188 measurements and operated at 20 kV and 6 nA in a focused beam configuration with a 70°
189 tilted stage and variable pressure (25 Pa) mode, which allows the study of uncoated
190 specimens. EBSD patterns of the kangite grains were indexed against structures of synthetic
191 Sc₂O₃ (Schleid and Meyer 1989), ScTiO₃ (Shafi et al. 2012), Sc₂TiO₅ (Kolitsch & Tillmanns
192 2003), Ti₂O₃ (Vincent et al. 1980), and perovskite CaTiO₃ (Liu & Liebermann 1993), and the
193 minerals panguite (Ti⁴⁺,Sc,Al,Mg,Zr,Ca)_{1.8}O₃ (IMA 2010-057; Ma et al. 2012), and
194 tazheranite (Zr,Ti,Ca)O_{1.75} (cubic zirconia; Rastsvetaeva et al. 1998). Among these, the
195 patterns can be indexed using a bixbyite-type structure (Sc₂O₃, ScTiO₃), a bixbyite-type

196 related structure (panguite), and a fluorite-type structure (tazheranite). Since the bixbyite
197 structure can be derived from a fluorite-structured oxide through a systematic removal of
198 oxygens, it follows that the EBSD data suggest a fluorite- or defective fluorite-structure.

199 Synchrotron micro-Laue diffraction on one kangite domain was carried out at the
200 34ID-E undulator beamline of the Advanced Photon Source in the Argonne National
201 Laboratory using a $250 \times 400 \text{ nm}^2$ polychromatic X-ray beam and an array of Perkin-Elmer
202 amorphous Si area detectors, using methods described in detail by Ma et al. (2012) in our
203 study of the newly discovered Sc-bearing Ti-oxide panguite. An energy scan (energy range
204 16 to 27 keV, 1 eV steps) of the primary beam yielded a set of 16 reflections, which were
205 used for a reverse Monte Carlo optimization (Endeavour 1.4; Puetz et al. 1999) with the
206 Sc_2O_3 C-type (bixbyite-type) structure as the initial configuration. The rMC optimization
207 converged to $R_{\text{Bragg}} = 0.079$ for the cubic bixbyite-type structure (see Deposited Item).
208 Subsequently we used SHELXL (Sheldrick 2008) for refinement. Isotropic atomic
209 displacement (U_{iso}) values, site occupancy factors (SOFs) of Sc1, Sc2, and x,y,z coordinates
210 for the cation and oxygen sites are given in Table 2. Refinement of the U_{iso} values, SOFs and
211 fractional coordinates was conducted in sequential steps.

212 Kangite shows a cation-deficient $Ia\bar{3}$ bixbyite-type structure with unit cell dimension
213 $a = 9.842(1) \text{ \AA}$, $V = 953.3(1) \text{ \AA}^3$, $Z = 16$. The EBSD pattern (Fig. 6) is an excellent match to
214 the computed EBSD pattern obtained using the cell parameter of the cubic structure from the
215 synchrotron micro-diffraction analysis with resulting mean angular deviations as low as 0.35.
216 X-ray powder-diffraction data (Table 3, in $\text{CuK}\alpha 1$, in Bragg-Brentano geometry) were
217 calculated using PowderCell (Kraus and Nolze 1996) version 2.4. Cation-cation distances in
218 kangite are around 2.6% larger than in synthetic Sc_2O_3 (Schleid and Meyer 1989). Isotropic
219 thermal displacement factors of the 8a and the 24d cations are similar, 0.017 and 0.015 in
220 synthetic Sc_2O_3 (Schleid and Meyer 1989) versus 0.012 and 0.009 in kangite (Table 2),
221 respectively. However, thermal displacement of oxygen is significantly larger in kangite than
222 in synthetic Sc_2O_3 : 0.16 versus 0.019 \AA^2 . We relate this observation to another important
223 difference between the structures of kangite and synthetic pure Sc_2O_3 . In both kangite and
224 pure Sc_2O_3 , cations residing at site 8a have six next neighbor anions, although cation-anion
225 distances are 5% shorter in kangite than in pure Sc_2O_3 . In synthetic Sc_2O_3 the cation on site
226 24d has six-fold coordination with Sc-O distances ranging from 2.08 to 2.17 \AA , as expected
227 for bixbyite-type phases (Wyckoff 1960). In kangite, however, two apices of the 24d centered
228 polyhedron are clearly beyond Sc-O bond distances, leaving Sc with an apparent four-fold

229 coordination. The four shortest cation-O distances range from 1.8 to 2.2 Å with the other two
230 at 3.0 and 3.5 Å. Obviously, bond orbital distributions still require a 6 - 8 fold coordination of
231 the major cations (Sc, Ti, Zr, etc.). These unusual observations can be explained by the high
232 density of cation vacancies in kangite and the fact that site occupancies for the 8a and 24d
233 sites are quite different. The 24d site has only 60% occupancy whereas the 8a site has 80%
234 occupancy. It is therefore likely that cations in the 8a site attract O closer in unit cells for
235 which the 24d site is empty than in those for which 24d is occupied. In the averaged structure
236 sampled by the micro-Laue measurements, this results in an overall shift of the O-atom
237 position away from the 24d site leaving the latter with an apparent incomplete coordination.
238 This interpretation is supported by the unusually large thermal displacement factor of O,
239 which is almost a factor of ten larger than in pure Sc₂O₃ (see above). In other words, this
240 large thermal displacement factor convolutes the static disorder of O atomic positions in
241 kangite. Such disorder can, in principle, be modeled by partial occupancies of multiple 48e
242 sites for O. However, such further refinement would require more unique reflections than are
243 available in our data set.

244 The structural relationships between kangite and panguite are very interesting because
245 of the similar compositions. Both phases are Ti-, Sc-rich oxides, whose compositions are well
246 expressed using a pseudobrookite-type formula M_3O_5 , but they reveal a bixbyite-type (M_2O_3)
247 or related structure. Kangite, which contains more Sc and significantly higher HREE
248 contents, has a bixbyite-type structure, whereas panguite shows a reduction in symmetry from
249 bixbyite-type $Ia\bar{3}$ to $Pbca$. In bixbyite and kangite, the cations assume two Wykhoff sites, 8a
250 and 24d, whereas the anion resides on the general position 48e. The cubic bixbyite structure
251 is related to the structure of panguite by a group-subgroup chain $Ia\bar{3} \rightarrow Ibca \rightarrow Pbca$ where
252 all atoms occupy the general site 8c (Aroyo et al. 2006). The reduced crystal symmetry of
253 panguite is the result of lattice relaxation due to the large number of vacancies and large
254 concentration of cations whose ionic radii are smaller than expected for a bixbyite-type structure.
255 This has been discussed in detail in Ma et al. (2012). Kangite has similarly large cation deficiency
256 but a larger concentration of REE elements, all of which establish end-member oxides in the
257 bixbyite structure. It is this higher concentration of large cations that stabilizes the bixbyite
258 structure for kangite. Cooling rates during the formation process may also play a role. However,
259 this can only be assessed by experimental studies on synthetic equivalents of kangite and
260 panguite.

261

262 *RAMAN SPECTROSCOPY*

263 Raman spectroscopic microanalysis was carried out using a Renishaw M1000 micro-
264 Raman spectrometer system on kangite domains of the sample in polished section, using the
265 methods described in Ma and Rossman (2008a, 2009a). Approximately 5 mW of 514.5 nm
266 laser illumination (at the sample) focused with a 100× objective lens provided satisfactory
267 spectra. The spot size was about 2 μm. The spectrum of kangite is characterized by intense
268 fluorescence features, similar to those of nearby perovskite grains, as shown in Figure 7. The
269 dominant Raman feature of synthetic Sc₂O₃ at 419 cm⁻¹ (Ubal dini and Carnasciali 2008) is
270 nearly invisible. The intense fluorescence features are due to significant amounts of
271 fluorescent *REE* elements in both kangite and perovskite (Table 1). Because features in the
272 Raman spectra arise from intense optical fluorescence due to the REE elements, there are no
273 identifiable Raman shifts and, hence, the spectra provide no information about the crystal
274 structure of the host phase.

275

276

DISCUSSION

277 Kangite is a new Sc-, Ti-rich oxide, (Sc,Ti,Al,Zr,Mg,Ca,□)₂O₃, with a *Ia* $\bar{3}$ bixbyite-
278 type structure, and a new member of the bixbyite group, which already contains bixbyite
279 (Mn₂O₃), avicennite (Ti₂O₃) and yttriaite-(Y) (Y₂O₃). It is the first mineral with a bixbyite-
280 type structure to be found in a meteorite. Kangite also joins a variety of Zr-, Y-, and Sc-rich
281 oxides and silicates, including allendeite, tazheranite, zirconolite, panguite, thortveitite,
282 lakargiite, eringaite, and davisite, that have been reported in refractory inclusions from
283 carbonaceous chondrites (Allen et al. 1980; Hinton et al. 1988; El Goresy et al. 2002; Ma and
284 Rossman 2008b, 2009b; Ma et al. 2009, 2011; Ma 2011; Ma 2012; Ma et al. 2012). Each of
285 these phases is a potential sensor of environment and kangite has the added advantage of
286 being heavy rare earth enriched and, therefore, potentially sensitive to condensation and
287 evaporative processes.

288 The juxtaposition of kangite, which has little if any Ti³⁺, within an aggregate of
289 davisite crystals whose Ti is largely trivalent, presents a challenge for understanding the
290 origin of kangite. There are three basic possibilities: (1) kangite formed or equilibrated in an
291 oxidizing environment separate from the reducing environment necessary to produce davisite
292 and was later transported to the davisite (or vice versa); (2) davisite and kangite both form
293 under reducing conditions but kangite discriminates against Ti⁺³ in much the same way that
294 perovskite, which is also present in this inclusion, does; (3) kangite originally formed as a

295 Ti^{3+} -enriched phase that was incorporated into the davisite aggregate but these original grains
296 were later oxidized at low temperatures (too low to affect the davisite) to form kangite.

297 Phase equilibria place basic constraints on the stability of a mineral and the conditions
298 under which it may have formed. For kangite, the most relevant binary system under
299 oxidizing conditions is Sc_2O_3 - TiO_2 but the phase relations of Sc_2O_3 - TiO_x -bearing systems in
300 general and of bixbyite-structured oxides within these systems in particular are poorly
301 constrained. The high temperature phase diagram of Magunov and Magunov (2002) for the
302 system Sc_2O_3 - TiO_2 shows a solubility of only a few mole % TiO_2 in the terminal Sc_2O_3 solid
303 solution (their data constrain it to < 10 mole%) with greater amounts of TiO_2 generating
304 Sc_2TiO_5 up to the melting point of that compound at 1347°C. Although they did not note it,
305 the compound $\text{Sc}_4\text{Ti}_3\text{O}_{12}$ (e.g., Lyashenko et al. 2004) also appears to be stable in this system
306 at high temperatures. There are also some constraints on phase stabilities for compositions
307 within the quaternary Sc_2O_3 - TiO_2 - Y_2O_3 - ZrO_2 (e.g., Tao and Irvine 2002) but the
308 experimentally examined compositions are far richer in Y+Zr (≥ 65 mole % of the cations for
309 Tao and Irvine's study) than in kangite ($\sim 10\%$; Fig. 4). Kangite has not been synthesized to
310 our knowledge but many trivalent end-member oxides are known to assume a bixbyite
311 structure, including Sc_2O_3 , Y_2O_3 , trivalent oxides of the rare earths, and In_2O_3 . Available data
312 for Sc_2O_3 - TiO_2 imply that a bixbyite structured scandian oxide as TiO_2 -rich as kangite (molar
313 $\text{Ti}/\text{Sc} \sim 1.2$) is not a stable high temperature phase under oxidizing conditions relative to a
314 Sc_2TiO_5 - or $\text{Sc}_4\text{Ti}_3\text{O}_{12}$ -bearing phase assemblage. This argues against scenario (1) given at
315 the beginning of this section and for a low temperature origin. If kangite is a high temperature
316 phase produced under oxidizing conditions, then one or more of the other cations present in
317 significant concentrations (i.e., Al, Zr, Mg, and/or Ca) must have stabilized the bixbyite
318 structure.

319 It is important to consider the possible role of Ti^{3+} in the origin of kangite, both from
320 the perspective of whether or not kangite can accommodate Ti^{3+} (e.g., scenario 2) and what
321 the nature and stability of a Ti^{3+} -enriched precursor would have been (scenario 3). The
322 average ionic radius of trivalent cations in kangite is 0.70 Å and, if Si is removed from the
323 formula in the form of davisite (i.e., all Si in the kangite analysis is due to contamination of
324 the activation volumes for EPMA by the surrounding davisite), then the average ionic radius
325 is 0.67 Å. Moreover, trivalent cations present in significant concentrations (Al, Sc, Y) have
326 ionic radii ranging from 0.53 to 0.89 Å. The ionic radius of Ti^{3+} is 0.67 Å, near the average,
327 which implies that there are no large size-related energetic penalties associated with the
328 substitution of Ti^{3+} into kangite. Thus, scenario (2) is unlikely. Kangite discriminated against

329 Ti^{3+} because there was little or none to be had at the time it formed. Kangite formed (or
330 equilibrated) in an oxidizing environment separate from the one that produced the davisite.

331 If kangite is the oxidized form of a Ti^{3+} -enriched precursor (scenario 3), then phase
332 relations in the system Sc_2O_3 - Ti_2O_3 are pertinent to the origin of the precursor but these are
333 even less well constrained than for Sc_2O_3 - TiO_2 . Ti_2O_3 , which takes on a corundum-type
334 structure ($R\bar{3}c$), can be synthesized with up to 4 mole % Sc_2O_3 (Chandrashekar et al. 1974)
335 and the double oxide $\text{ScTi}^{+3}\text{O}_3$, which has a bixbyite-type structure, is readily synthesized at
336 high temperatures under reducing conditions (Reid and Sienko 1967). The solubility of Ti_2O_3
337 in a terminal Sc_2O_3 solution is unknown but, given that bixbyite-type structures tend to be
338 mostly sensitive to ionic radius for a potential substituting cation, it seems likely that the
339 solubility is significantly greater than that of Sc in tistarite (Ti_2O_3). Even these limited
340 observations place an important constraint on the origin of kangite. A kangite precursor
341 could, in principle have been an $M_2\text{O}_3$ oxide but, given the low solubility of Sc in Ti_2O_3 , it
342 was not tistarite.

343 Although there is a paucity of phase equilibrium data for kangite composition oxides
344 and Ti^{3+} -enriched analogs, there is a substantial literature concerning the solubility
345 relationships and energetics of solid solutions of bixbyite-type structured oxides. Systems
346 involving In_2O_3 are the most heavily studied because of their use in energy efficient windows,
347 flat screen panel displays and an assortment of photovoltaics but there are enough data on
348 enough systems (e.g., Busker et al. 1999; Freeman et al. 2000; Saha et al. 2002; Mason et al.
349 2003; Levy et al. 2007; Hoel et al. 2010) to allow for the expression of some general
350 principles regarding the substitution of cations into a bixbyite structured end-member $M_2\text{O}_3$
351 oxide such that the $Ia\bar{3}$ space group is retained: (1) for an aliovalent substitution (i.e., a 3+
352 cation substituting for a 3+ cation), cations with ionic radii similar to those of the host are
353 energetically favored; (2) substitution of a single type of divalent or tetravalent cation for a
354 3+ host is compensated by oxygen interstitials or cation vacancies (for kangite this would
355 likely be via cation vacancies); (3) co-doping of 4+ and 2+ cations substantially enhances the
356 solubility of both cations relative to the solubility of either by itself; and (4) the solubility of
357 co-doped 4+ and 2+ cations is maximized when the average ionic radius of the two cations
358 approaches that of the host.

359 Consider a reduced precursor to kangite (scenario 3) in light of the above four
360 principles. We begin with the premise that Si is a contaminant from davisite, although it is
361 possible that Si is soluble in small amounts in kangite. As shown above, removing the Si by

362 subtracting davisite and renormalizing to a 3 oxygen basis leads to the kangite formula:

363 $[(\text{Sc}_{0.54}\text{Al}_{0.16}\text{Y}_{0.07}\text{V}_{0.03}\text{Gd}_{0.01}\text{Dy}_{0.01}\text{Er}_{0.01})^{3+}_{\Sigma 0.83}(\text{Ti}_{0.66}\text{Zr}_{0.13})^{4+}_{\Sigma 0.79}(\text{Mg}_{0.11}\text{Ca}_{0.06}\text{Fe}_{0.02})^{2+}_{\Sigma 0.19}\square_{0.19}$

364 $]\Sigma_{2.00}\text{O}_3$. This formula has slightly lower Al and Ca (and no Si) than the measured kangite

365 composition as given in Table 1 because these cations are in much greater abundance in

366 davisite than in kangite. There are 0.79 quadrivalent cations in this formula unit but only 0.19

367 divalent cations, which means that there are far more 4+ cations than can be accommodated

368 through co-doping of 2+ and 4+ cations. This is equivalent to saying that there are far more

369 Ti^{4+} cations than can be accounted for through co-doping. As an end-member model, we

370 assume that all 4+ cations are co-doped with 2+ cations in the kangite precursor and that all

371 remaining Ti in the kangite precursor was trivalent. This yields a formula unit of

372 $[(\text{Ti}_{0.61}\text{Sc}_{0.53}\text{Al}_{0.19}\text{Y}_{0.06}\text{V}_{0.02}\text{Gd}_{0.01}\text{Dy}_{0.01}\text{Er}_{0.01})^{3+}_{\Sigma 1.44}(\text{Ti}_{0.05}\text{Zr}_{0.14})^{4+}_{\Sigma 0.19}(\text{Mg}_{0.11}\text{Ca}_{0.06}\text{Fe}_{0.02})^{2+}_{\Sigma 0.19}$

373 $]\Sigma_{2.00}\text{O}_3$ for the kangite precursor. Note that this phase has an even higher $\text{Ti}^{3+}/\text{Ti}^{4+}$ ratio (12)

374 than does davisite (2). Of course, intermediate formulae can be constructed in which some

375 fraction of the Ti that is not co-doped with a divalent cation is accommodated as Ti^{4+} in the

376 precursor through cation defects or interstitial oxygen. Ti^{4+} (0.605 Å) has a significantly lower

377 ionic radius than does Sc (0.73 Å) or Ti^{3+} (0.67 Å) but the average ionic radius for a Ca: Ti^{4+}

378 co-doping couple is higher (0.80 Å) than the average ionic radius for the trivalent cations

379 though still smaller than that of Y (0.89 Å), which is present in kangite in similar

380 concentrations. Perhaps Al, which has a much lower ionic radius (0.53 Å) than those of Sc or

381 Ti^{3+} , partially stabilizes the structure for Ca: Ti^{4+} co-doping by reducing the mean ionic radius

382 for the mineral. Connecting the proposed precursor composition to specific redox conditions

383 would require additional experimentation but we can say that Ti^{3+} enriched precursors to

384 kangite are consistent with reducing conditions and that they may have formed in an

385 environment similar to or directly related to the one that produced the host davisite. The

386 structure of the kangite precursor is uncertain but the fact that cations of $\text{Ti}^{3+} \sim \text{Sc}^{3+}$ in the

387 davisite-corrected formula unit given above suggests the possibility that this may have been

388 an ScTiO_3 bixbyite- type phase with considerable solid solution towards various other

389 components. Alternatively, the inferred Ti:Sc ratio is fortuitous and the kangite precursor was

390 a terminal Sc_2O_3 solid solution. Both phases have a bixbyite-type structure. The kangite

391 precursor, which may well have been a high temperature condensate, was incorporated into

392 the host davisite aggregate but, at a presumably later time, the 0.6 cations of Ti^{3+} on a 3

393 oxygen basis, that was originally present, was oxidized to form 0.6 cations of Ti^{4+} and the

394 phase transformed into kangite. Shafi et al. (2012) showed that Ti^{3+} in $\text{ScTi}^{3+}\text{O}_3$ is readily

395 oxidized at low temperatures to form a metastable intermediate with a stoichiometry of
396 $\text{Sc}_2\text{Ti}^{4+}_2\text{O}_7$, which has a defect fluorite structure. A similar process may have occurred with
397 the kangite precursor but this phase, having only half the Ti^{3+} present in the end-member
398 ScTiO_3 could only be oxidized to an overall $M_3\text{O}_5$ (i.e., pseudobrookite-like) stoichiometry
399 and it therefore assumed or retained the bixbyite structure, as observed for kangite. The
400 oxidation process must have occurred at a sufficiently low temperature so that the kangite, so
401 produced, did not break down to form other, more stable oxides and davisite was unaffected.
402 We can place some constraints on the conditions for this process through a consideration of
403 CAIs in Allende. Based on alloy-oxide equilibria, the alloys in Allende CAIs were oxidized
404 at temperatures in the vicinity of $\sim 500^\circ\text{C}$ under conditions about a log unit more oxidizing
405 than the iron-wüstite buffer (e.g., Blum et al. 1989). During this event, clinopyroxene was
406 unaffected but iron diffused into the centers of large, 40-60 μm diameter, spinel grains from
407 the core region of an Allende type B inclusion, hundreds of μm from the surface of the CAI
408 (Paque et al. 2007). Spinel in the kangite bearing inclusion described here is very iron rich
409 (11.2 wt % FeO) and it is likely that this Fe was introduced during the Allende metasomatic
410 event. Given the close proximity of kangite crystals ($\leq 20 \mu\text{m}$ from the surface of the host
411 inclusion), the small grain size (2-12 μm) of the davisite (hence many grain boundaries that
412 could act as fast pathways for diffusion from the external medium outside the inclusion to the
413 surfaces of the kangite precursors), the small grain size of the kangite (1-4 μm grain sizes but
414 not more than $\sim 2 \mu\text{m}$ thick; see Fig. 2), and the highly ferroan compositions of nearby and
415 kangite-contacting spinel in the same inclusion, it is virtually certain that the kangite
416 precursor would have been exposed to these oxidizing metasomatic conditions. If so, the low
417 concentration of Fe in kangite suggests that the solubility of Fe^{2+} was very low compared to
418 spinel exposed to virtually identical conditions (cf., Table 1). This is consistent with the
419 absence of exchangeable Ti^{4+} from other phases during the alteration process that would have
420 been necessary to charge balance the substitution of Fe^{2+} into kangite.

421 We conclude that kangite most likely formed as the low-temperature oxidation
422 product of a Sc-, Ti^{3+} -enriched oxide that formed under reducing conditions, presumably as a
423 condensate and probably with a bixbyite-type structure. Note that this high temperature
424 precursor, were it to be found, would be a new mineral. It would not be kangite because
425 cations of $\text{Ti}^{3+} > \text{Sc}$ and it would not be tistarite because it would have a different structure.
426 This reduced kangite precursor was incorporated into an aggregate of davisite crystals along
427 with small amounts of perovskite and spinel and it was later oxidized to form kangite. It is

428 possible that the oxidation event occurred prior to incorporation into the davisite aggregate
429 (i.e., the grains arrived as kangite crystals) but the most straightforward scenario is one in
430 which the same metasomatic event that introduced iron into spinels, including the ones shown
431 in Figures 1-2, and oxidized metal in Allende CAIs, also caused in situ oxidation of the
432 kangite precursor. If so, the composition of the kangite, except for oxygen and possibly Fe,
433 approximates that of the original precursor and, because there were ≤ 0.6 cations of Ti^{3+} per 3
434 oxygens in the original crystals, oxidation yielded a roughly M_3O_5 stoichiometry and a
435 bixbyite-type structure was retained.

436 Although we have emphasized the origin of kangite in this discussion, it is also
437 important to place the proposed Ti^{3+} -enriched precursor into a broader cosmochemical
438 context. Both kangite and perovskite in the inclusion described in this study are highly
439 enriched in HREE (Fig. 5) and this provides a key to understanding their origin. In general,
440 ultrarefractory inclusions are characterized by extraordinarily high HREE/LREE ratios and
441 negative Yb anomalies as shown in Figure 5. Only a handful of meteoritic inclusions with
442 ultrarefractory REE patterns have been described (e.g., Davis 1984; 1991; Simon et al. 1996;
443 El Goresy et al. 2002; Uchiyama et al. 2008) but Boynton (1975) proposed their existence
444 before any had been discovered based on thermodynamic modeling of high temperature
445 condensation. Moreover, the absence of isotopic mass fractionation in Ti and Mg in at least
446 one of these inclusions suggests that the ultrarefractory grains are condensates rather than
447 evaporative residues (Simon et al. 1996). Some meteoritic inclusions (described as Group II)
448 appear to have derived their REE budget via condensation from a reservoir that was depleted
449 in an ultrarefractory component. Group II inclusions are fairly common among CAIs and
450 especially common among fine-grained inclusions (Davis 1991; Hiyagon et al. 2011).
451 Ultrarefractory phases, including perovskite and the kangite precursor from this study, are
452 representatives of solid extracts from high temperature fractional condensation processes.
453 Although the occurrence of ultrarefractory material as original condensate grains is rare, its
454 effect is often observed through REE patterns of lower temperature condensates that are
455 missing an ultrarefractory component.

456

457

ACKNOWLEDGEMENTS

458 SEM, EBSD and EPMA analyses were carried out at the Caltech GPS Division
459 Analytical Facility, which is supported, in part, by NSF Grants EAR-0318518 and DMR-
460 0080065. Synchrotron micro-diffraction was carried out at the 34ID-E beamline of the
461 Advanced Photon Source. Use of the Advanced Photon Source, an Office of Science User

462 Facility operated for the U.S. Department of Energy (DOE) Office of Science by Argonne
463 National Laboratory, was supported by the U.S. DOE under Contract No. DE-AC02-
464 06CH11357. This research was also supported by NASA Cooperative Agreement DE-FC88-
465 01NV14049, NASA OSS Grant NNX09AG40G, and NSF Grant EAR-0947956. We thank
466 A.M. Davis, M. Kimura, R.C. Peterson, and associate editor R.H. Jones for constructive and
467 helpful reviews.

468
469
470

REFERENCES

- 471 Allen, J.M., Grossman, L., Davis, A.M., and Hutcheon, I.D. (1978) Mineralogy, textures and
472 mode of formation of a hibonite-bearing Allende inclusion. Proceedings of the 9th Lunar
473 and Planetary Science Conference, 1209-1233.
- 474 Allen, J.M., Grossman, L., Lee, T., and Wasserburg, G.J. (1980) Mineralogy and petrography
475 of HAL, an isotopically-unusual Allende inclusion. *Geochimica et Cosmochimica Acta*,
476 44, 685-699.
- 477 Anders, E. and Grevesse, N. (1989) Abundances of the elements. *Geochimica et*
478 *Cosmochimica Acta*, 53, 197-214.
- 479 Armstrong, J.T., Hutcheon, I.D., and Wasserburg, G.J. (1987) Zeldia and company:
480 Petrogenesis of sulfide-rich Fremdlinge and constraints on solar nebula processes.
481 *Geochimica et Cosmochimica Acta*, 51, 3155-3173.
- 482 Armstrong, J.T. (1995) CITZAF: a package of correction programs for the quantitative
483 electron microbeam X-ray analysis of thick polished materials, thin films, and particles.
484 *Microbeam Analysis*, 4, 177-200.
- 485 Aroyo, M.I., Perez-Mato, J.M., Capillas, C., Kroumova, E., Ivantchev, S., Madariaga, G.,
486 Kirov, A., and Wondratschek, H. (2006) Bilbao Crystallographic Server: I. Databases
487 and crystallographic computing programs. *Zeitschrift für Kristallographie*, 221, 15-27.
- 488 Blum, J.D., Wasserburg, G.J., Hutcheon, I.D., Beckett, J.R., and Stolper, E.M. (1989) Origin
489 of opaque assemblages in C3V meteorites: Implications for nebular and planetary
490 processes. *Geochimica et Cosmochimica Acta*, 53, 543-556.
- 491 Boynton, W.V. (1975) Fractionation in the solar nebula: condensation of yttrium and the rare
492 earth elements. *Geochimica et Cosmochimica Acta*, 39, 569-584.
- 493 Busker, G., Chroneos, A., Grimes, R.W., and Chen, I.W. (1999) Solution mechanisms for
494 dopant oxides in yttria. *Journal of the American Ceramic Society*, 82, 1553-1559.

- 495 Chandrashekar, G.V., Van Zandt, L.L., Honig, J.M., and Jayaraman, A. (1974) Electrical
496 properties and the metal-insulator transition in $(\text{Sc}_x\text{Ti}_{1-x})_2\text{O}_3$. *Physical Review B*, 10,
497 5063-5068.
- 498 Clarke, R.S., Jarosewich, E., Mason, B., Nelen, J., Gómez, M., and Hyde, J.R. (1971) The
499 Allende, Mexico, meteorite shower. *Smithsonian Contributions to Earth Science*, 5, 1-53.
- 500 Connolly, H.C. and Burnett, D.S. (1999) A study of the minor element concentrations of
501 spinels from two type B calcium-aluminum-rich inclusions: An investigation into
502 potential formation conditions of calcium-aluminum-rich inclusions. *Meteoritics &*
503 *Planetary Science*, 34, 829-848.
- 504 Connolly, H.C., Burnett, D.S., and McKeegan, K.D. (2003) The petrogenesis of type B1 Ca-
505 Al-rich inclusions: The spinel perspective. *Meteoritics & Planetary Science*, 38, 197-
506 224.
- 507 Davis, A.M. (1984) A scandalously refractory inclusion in Ornans. *Meteoritics* 19, 214.
- 508 Davis, A.M. (1991) Ultrarefractory inclusions and the nature of the group II REE
509 fractionation. *Meteoritics*, 26, 330.
- 510 El Goresy, A., Armstrong, J.T., and Wasserburg, G.J. (1985) Anatomy of an Allende coarse-
511 grained inclusion. *Geochimica et Cosmochimica Acta*, 49, 2433-2444.
- 512 El Goresy, A., Zinner, E., Matsunami, S., Palme, H., Spettel, B., Lin, Y., and Nazarov, M.
513 (2002) Efremovka 101.1: A CAI with ultrarefractory REE patterns and enormous
514 enrichments of Sc, Zr, and Y in fassaite and perovskite. *Geochimica et Cosmochimica*
515 *Acta*, 66, 1459-1491.
- 516 Freeman, A.J., Poeppelmeier, K.R., Mason, T.O., Chang, R.P.H., and Marks, T.J. (2000)
517 Chemical and film strategies for new transparent conducting oxides. *MRS Bulletin*, 25,
518 45-51.
- 519 Hatert, F. and Burke, E.A.J. (2008) The IMA-CNMNC dominant-constituent rule revisited
520 and extended. *Canadian Mineralogist*, 46, 717-728.
- 521 Hinton, R.W., Davis, A.M., Scatena-Wachel, D.E., Grossman, L., and Draus, R.J. (1988) A
522 chemical and isotopic study of hibonite-rich refractory inclusions in primitive meteorites.
523 *Geochimica et Cosmochimica Acta*, 52, 2573-2598.
- 524 Hiyagon, H., Yamakawa, A., Ushikubo, T., Lin, Y., and Kimura, M. (2011) Fractionation of
525 rare earth elements in refractory inclusions from the Ningqiang meteorite: Origin of
526 positive anomalies in Ce, Eu, and Yb. *Geochimica et Cosmochimica Acta*, 75, 3358-
527 3384.

- 528 Hoel, C.A., Gaillard, J.-F., and Poeppelmeier, K.R. (2010) Probing the local structure of
529 crystalline ZITO: $\text{In}_{2-2x}\text{Sn}_x\text{Zn}_x$ ($x \leq 0.4$) *Journal of Solid State Chemistry* 183, 761-768.
- 530 Kolitsch, U. and Tillmanns, E. (2003) Sc_2TiO_5 , an entropy-stabilized pseudobrookite-type
531 compound. *Acta Crystallographica*, E59, i36-i39.
- 532 Kraus, W. and Nolze, G. (1996) POWDER CELL – a program for the representation and
533 manipulation of crystal structures and calculation of the resulting X-ray powder patterns.
534 *Journal of Applied Crystallography*, 29, 301-303.
- 535 Krot, A.N., MacPherson, G.J., Ulyanov, A.A., and Petaev, M.I. (2004) Fine-grained, spinel-
536 rich inclusions from the reduced CV chondrites Efremovka and Leoville: I. Mineralogy,
537 petrology, and bulk chemistry. *Meteoritics & Planetary Science*, 39, 1517-1553.
- 538 Levy, M.R., Stanek, C.R., Chroneos, A., and Grimes, R.W. (2007) Defect chemistry of doped
539 bixbyite oxides. *Solid State Sciences*, 9, 588-593.
- 540 Liu, X. and Liebermann, R.C. (1993) X-ray powder diffraction study of CaTiO_3 perovskite at
541 high temperatures. *Physics and Chemistry of Minerals*, 20, 171-175.
- 542 Lovering, J.F., Wark, D.A., and Sewell, D.K.B. (1979) Refractory oxide, titanate, niobate and
543 silicate accessory mineralogy of some type B Ca-Al-rich inclusions in the Allende
544 meteorite. *Lunar and Planetary Science*, 10, 745-746.
- 545 Lyashenko, L.P., Kolbanov, I.V., Shcherbakova, L.G., Knerel'man, E.I., and Davydova, G.I.
546 (2004) Effect of nonequilibrium state on phase relations in the system $\text{TiO}_2\text{-Sc}_2\text{O}_3$ (40-50
547 mol % Sc_2O_3). *Inorganic Materials*, 40, 833-839.
- 548 Ma, C. and Rossman, G.R. (2008a) Barioperovskite, BaTiO_3 , a new mineral from the
549 Benitoite Mine, California. *American Mineralogist*, 93, 154-157.
- 550 Ma, C. and Rossman, G.R. (2008b) Discovery of tazheranite (cubic zirconia) in the Allende
551 meteorite. *Geochimica et Cosmochimica Acta*, 72, 12S, A577.
- 552 Ma, C. and Rossman, G.R. (2009a) Tistarite, Ti_2O_3 , a new refractory mineral from the
553 Allende meteorite. *American Mineralogist*, 94, 841-844.
- 554 Ma, C. and Rossman, G.R. (2009b) Davisite, CaScAlSiO_6 , a new pyroxene from the Allende
555 meteorite. *American Mineralogist*, 94, 845-848.
- 556 Ma, C., Beckett, J.R., and Rossman, G.R. (2009) Allendeite and hexamolybdenum: Two new
557 ultra-refractory minerals in Allende and two missing links. *Lunar and Planetary Science*
558 40, Abstract # 1402.
- 559 Ma, C. (2011) Discovery of meteoritic lakargiite (CaZrO_3), a new ultra-refractory mineral
560 from the Acfer 094 carbonaceous chondrite. *Meteoritics & Planetary Science*, 46 (S1),
561 A144.

- 562 Ma, C., Beckett, J.R., Tschauner, O., and Rossman, G.R. (2011) Thortveitite ($\text{Sc}_2\text{Si}_2\text{O}_7$), the
563 first solar silicate? *Meteoritics & Planetary Science*, 46 (S1), A144.
- 564 Ma, C. (2012) Discovery of meteoritic eringaite, $\text{Ca}_3(\text{Sc,Y,Ti})_2\text{Si}_3\text{O}_{12}$, the first solar garnet?
565 *Meteoritics & Planetary Science*, 47 (S1), A256.
- 566 Ma, C., Tschauner, O., Beckett, J.R., Rossman, G.R., and Liu, W. (2012) Panguite,
567 $(\text{Ti}^{4+},\text{Sc,Al,Mg,Zr,Ca})_{1.8}\text{O}_3$, a new ultra-refractory titania mineral from the Allende
568 meteorite: Synchrotron micro-diffraction and EBSD. *American Mineralogist*, 97, 1219-
569 1225.
- 570 Magunov, R.L., and Magunov, I.R. (2002) The system Sc_2O_3 - TiO_2 (in Russian). *Ukrainian*
571 *Journal of Chemistry*, 68, 85-88.
- 572 Mason, T.O., Kammler, D.R., Ingram, B.J., Gonzalez, G.B., Young, D.L., and Coutts, T.J.
573 (2003) Key structural and defect chemical aspects of Cd-In-Sn-O transparent conducting
574 oxides. *Thin Solid Films*, 445, 186-192.
- 575 Noonan, A.F., Nelen, J., Fredriksson, K., and Newbury, D. (1977) Zr-Y oxides and high-
576 alkali glass in an amoeboid inclusion from Ornans. *Meteoritics*, 12, 332-333.
- 577 Paque, J.M., Burnett, D.S., and Beckett, J.R. (2007) Zoning patterns of Fe and V in spinel
578 from a type B Ca-Al-rich inclusion: Constraints on subsolidus thermal history.
579 *Meteoritics & Planetary Science*, 42, 899-912.
- 580 Paque, J.M., Sutton, S.R., Burnett, D.S., Beckett, J.R., and Simon, S.B. (2010) An intimate
581 mix of highly oxidizing and highly reducing environments: relict spinel determined by
582 XANES in a partially melted Allende Ca-Al-rich inclusion. *Lunar and Planetary Science*
583 41, Abstract # 1391.
- 584 Puetz, H., J.C. Schön, J.C. and Jansen, M. (1999) Combined method for *ab initio* structure
585 solution from powder diffraction data. *Journal of Applied Crystallography*, 32, 864-870.
- 586 Rastsvetaeva, R.K., Pushcharovskii, D.Yu., Spiridonov, E.M., and Gekimyants, V.M. (1998)
587 Tazheranite and calzirtite: structural-mineralogical similarity and distinction. *Doklady*
588 *Akademii Nauk SSSR*, 359, 529-531.
- 589 Reid, A.F. and Sienko, M.J. (1967) Scandium titanite and vanadite, ScTiO_3 and ScVO_3 .
590 *Inorganic Chemistry*, 6, 521-524.
- 591 Saha, D., Das Sharma, A., Sen, A., and Maiti, H.S. (2002) Preparation of bixbyite phase
592 $(\text{Mn}_x\text{Fe}_{1-x})_2\text{O}_3$ for NTC thermistor applications. *Materials Letters*, 55, 403-406.
- 593 Shafi, S.P., Hernden, B.C., Cranswick, L.M.D., Hansen, T.C., and Bieringer, M. (2012)
594 Topotactic oxidation pathway of ScTiO_3 and high-temperature evolution of $\text{ScTiO}_{3.5}$ and
595 $\text{Sc}_4\text{Ti}_3\text{O}_{12}$ -type phases. *Inorganic Chemistry*, 51, 1269-1277.

- 596 Schleid, T. and Meyer, G. (1989) Single crystals of rare earth oxides from reducing halide
597 melts. *Journal of the Less-Common Metals*, 149, 73-80.
- 598 Sheldrick, G.M. (2008) A short history of SHELX. *Acta Crystallographica*, A64, 112-122.
- 599 Simon, S.B., Davis, A.M., and Grossman, L. (1996) A unique ultrarefractory inclusion from
600 the Murchison meteorite. *Meteoritics & Planetary Science*, 31, 106-115.
- 601 Simon, S.B., Sutton, S.R., Grossman, L. (2007) Valence of titanium and vanadium in
602 pyroxene in refractory inclusion interiors and rims. *Geochimica et Cosmochimica Acta*,
603 71, 3098-3118.
- 604 Srinivasan, G., Huss, G.R., and Wasserburg, G.J. (2000) A petrographic, chemical, and
605 isotopic study of calcium-aluminum-rich inclusions and aluminum-rich chondrules from
606 the Axtell (CV3) chondrite. *Meteoritics & Planetary Science*, 35, 1333-1354.
- 607 Tao, S. and Irvine, J.T.S. (2002) Optimization of mixed conducting properties of Y_2O_3 - ZrO_2 -
608 TiO_2 and Sc_2O_3 - Y_2O_3 - ZrO_2 - TiO_2 solid solutions as potential SOFC anode materials.
609 *Journal of Solid State Chemistry*, 165, 12-18.
- 610 Ubaldini, A. and Carnasciali, M.M. (2008) Raman characterisation of powder of cubic RE_2O_3
611 (RE = Nd, Gd, Dy, Tm, and Lu), Sc_2O_3 and Y_2O_3 . *Journal of Alloys and Compounds*,
612 454, 374-378.
- 613 Uchiyama, K., Hiyagon, H., Takahata, N., Sano, Y., Ushikubo, T., Kimura, M., and
614 Hashimoto, A. (2008) ion microprobe analyses of rare earth elements in an extremely
615 ultrarefractory nodule from the Efremovka CV3 chondrite. *Lunar and Planetary Science*,
616 39, Abstract #1519.
- 617 Vincent, M.G., Yvon, K., and Gruttner, A. (1980) Electron-density studies of metal-metal
618 bonds. I. The deformation density of Ti_2O_3 at 295 K. *Acta Crystallographica*, A36, 803-
619 808.
- 620 Wark, D.A. and Lovering, J.F. (1982) The nature and origin of type B1 and B2 Ca-Al-rich
621 inclusions in the Allende meteorite. *Geochimica et Cosmochimica Acta*, 46, 2581-2594.
- 622 Weber, D. and Bischoff, A. (1994) The occurrence of grossite ($CaAl_4O_7$) in chondrites.
623 *Geochimica et Cosmochimica Acta*, 58, 3855-3877.
- 624 Wyckoff, R.W.G. (1960) *Crystal Structures*. Interscience Publishers, New York. Volume 2.
625

626 **Table 1.** Mean electron microprobe analytical results for type kangite, associated perovskite,
 627 spinel, and host davisite.

Constituent	kangite	perovskite	davisite next to kangite and perovskite	davisite near the edge	spinel
wt%	n=7 ^a	n=6	n=6	n=2	n=6
TiO ₂	36.6(4) ^b	51.2(3)	8.9(6)	9.2(7)	0.42(2)
Sc ₂ O ₃	26.4(5)	0.8(2)	15(1)	9(1)	0.05(1)
ZrO ₂	11.3(3)	0.13(5)	2.1(5)	1.1(3)	b.d.
Al ₂ O ₃	7.0(2)	0.84(9)	22(2)	19.1(5)	65.75(7)
Y ₂ O ₃	5.4(1)	6.3(1)	0.8(1)	0.68(3)	b.d.
CaO	3.9(2)	31.3(2)	23.2(4)	23.70(2)	0.15(2)
MgO	3.14(6)	b.d. ^c	2(1)	5.4(5)	21.2(1)
SiO ₂	1.7(4)	b.d.	25(2)	31.1(7)	b.d.
V ₂ O ₃	1.31(4)	0.64(4)	0.53(2)	0.52(4)	0.38(1)
FeO	0.8(6)	0.61(2)	0.40(7)	0.43(7)	11.22(7)
Cr ₂ O ₃	0.09(2)	b.d.	b.d.	0.03(1)	0.30(1)
Dy ₂ O ₃	1.8(1)	3.1(1)	0.30(7)	0.25(4)	n.a. ^d
Er ₂ O ₃	0.92(5)	1.00(5)	0.10(5)	b.d.	n.a.
Gd ₂ O ₃	0.60(4)	2.52(7)	0.18(9)	0.14(2)	n.a.
Ho ₂ O ₃	0.40(2)	0.48(7)	b.d.	b.d.	n.a.
Tb ₂ O ₃	0.18(7)	0.40(6)	b.d.	b.d.	n.a.
ThO ₂	0.04(2)	0.40(6)	b.d.	b.d.	n.a.
O ^e	-0.3(2)	-0.3(2)			
Total	101.28	99.42	100.51	100.65	99.47

628
 629
 630
 631
 632
 633
 634
 635
 636
 637
 638
 639
 640
 641

^aNumber of analyses.

^bNumbers in parentheses represent one standard deviation of the mean for the n analyses conducted on the phase.

^cBelow detection. Detection limits at 99% confidence are Mg 0.09 wt%, Si 0.08 %, Cr 0.07 %, Zr 0.05%, Y 0.06%, Si 0.02%, Er 0.10%, Ho 0.09%, Tb 0.08%, Th 0.03%.

^dNot analyzed.

^eDifference between oxygen measured by EPMA and value obtained from elemental concentrations of cations as determined by EPMA in which a single valence (listed in the left hand column) has been assumed for each of the oxides. The quoted uncertainty reflects only the analytical error on the oxygen analysis.

642 **Table 2.** Atom coordinates.
643

	x/a	y/b	z/c	SOF	U_{iso}
644 Sc1	0.25	0.25	0.25	0.767(2)	0.012(3)
645 Sc2	0.9784(2)	0	0.25	0.590(1)	0.0093(3)
646 O	0.3207(6)	0.227(5)	-0.44(5)	1	0.16(9)

647
648
649

650 **Table 3.** Calculated X-ray powder diffraction data for kangite.
 651

652	<i>h</i>	<i>k</i>	<i>l</i>	<i>d</i> [Å]	<i>I</i> _{rel}
653	2	1	1	4.0190	16
654	2	2	2	2.8419	100
655	3	2	1	2.6311	1
656	4	0	0	2.4612	10
657	4	1	1	2.3204	5
658	4	2	0	2.2013	1
659	3	3	2	2.0989	15
660	4	2	2	2.0095	2
661	4	1	3	1.9307	75
662	5	2	1	1.7974	3
663	4	4	0	1.7403	51
664	4	3	3	1.6883	3
665	4	4	2	1.6408	1
666	6	1	1	1.5970	4
667	6	0	2	1.5566	1
668	5	4	1	1.5191	29
669	6	2	2	1.4841	23
670	6	1	3	1.4515	4
671	4	4	4	1.4210	2
672	5	4	3	1.3922	2
673	6	0	4	1.3652	1
674	7	2	1	1.3397	4
675	6	4	2	1.3155	1
676	6	1	5	1.2503	1
677	8	0	0	1.2306	4
678	8	1	1	1.2118	2
679	8	2	0	1.1938	1
680	6	5	3	1.1767	1
681	8	2	2	1.1602	1
682	8	3	1	1.1444	1
683	6	6	2	1.1293	6
684	8	0	4	1.1007	2
685	8	3	3	1.0869	1
686	8	2	4	1.0739	1
687	6	5	5	1.0613	2
688	6	6	4	1.0492	1
689	7	4	5	1.0374	1
690	7	6	3	1.0151	2
691	8	4	4	1.0045	5
692	9	4	1	0.9942	1
693	8	5	3	0.9942	2
694	8	6	0	0.9842	2
695	7	7	2	0.9745	1
696	8	2	6	0.9651	4
697	9	3	4	0.9559	1
698	10	2	2	0.9471	4
699	7	6	5	0.9384	1
700	8	5	5	0.9218	1

701
 702
 703

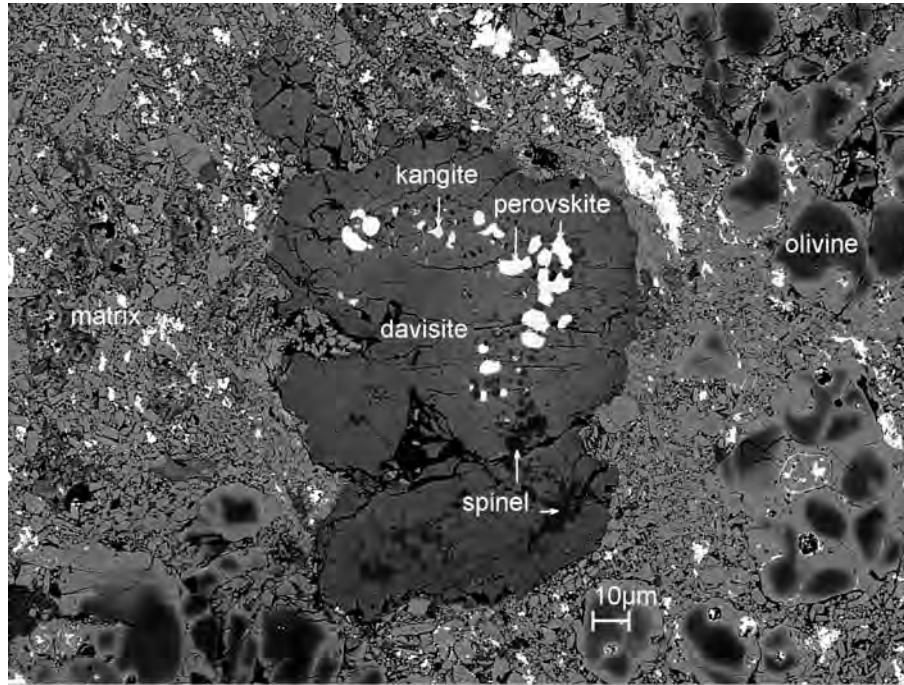
704
705
706
707
708
709
710
711
712
713
714
715
716
717
718
719
720
721

Deposited Item.

List of observed and calculated normalized structure factor moduli of unique reflections.*

<i>h</i>	<i>k</i>	<i>l</i>	F_o^2	F_c^2	$\sigma(F^2)/su$	$F_o/F_c(\max)$	Resolution (Å)
2	6	8	92916.11	56643.00	1.77	0.575	0.97
4	4	10	52273.38	41034.36	0.97	0.489	0.86
0	6	10	27150.91	32576.42	0.93	0.436	0.84
0	0	10	55806.35	56775.83	0.17	0.576	0.98
4	4	8	168947.70	171334.06	0.14	1.000	1.00

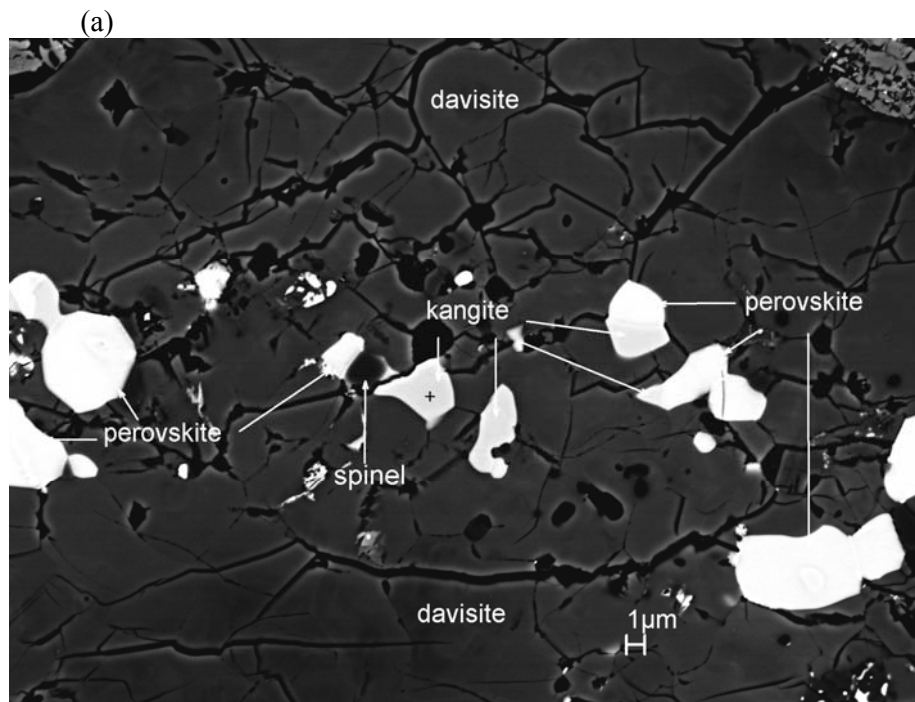
* $R_1 = 0.084$ for 5 unique reflections after merging; $wR2 = 0.139$, GooF 0.875 (Sheldrick 2008).



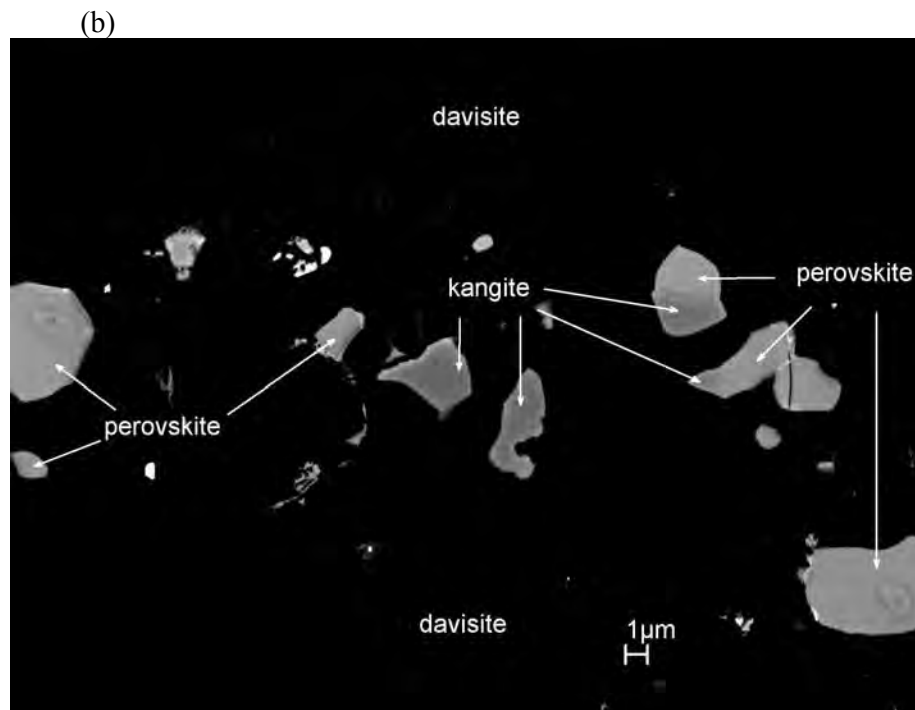
722
723
724
725
726
727
728

Figure 1. BSE image of ultrarefractory inclusion ACM-3 in section USNM 7555 from the Allende meteorite, where the type davisite (Ma and Rossman 2009b) and kangite (this study) occur. Scale bar is 10 μm .

729



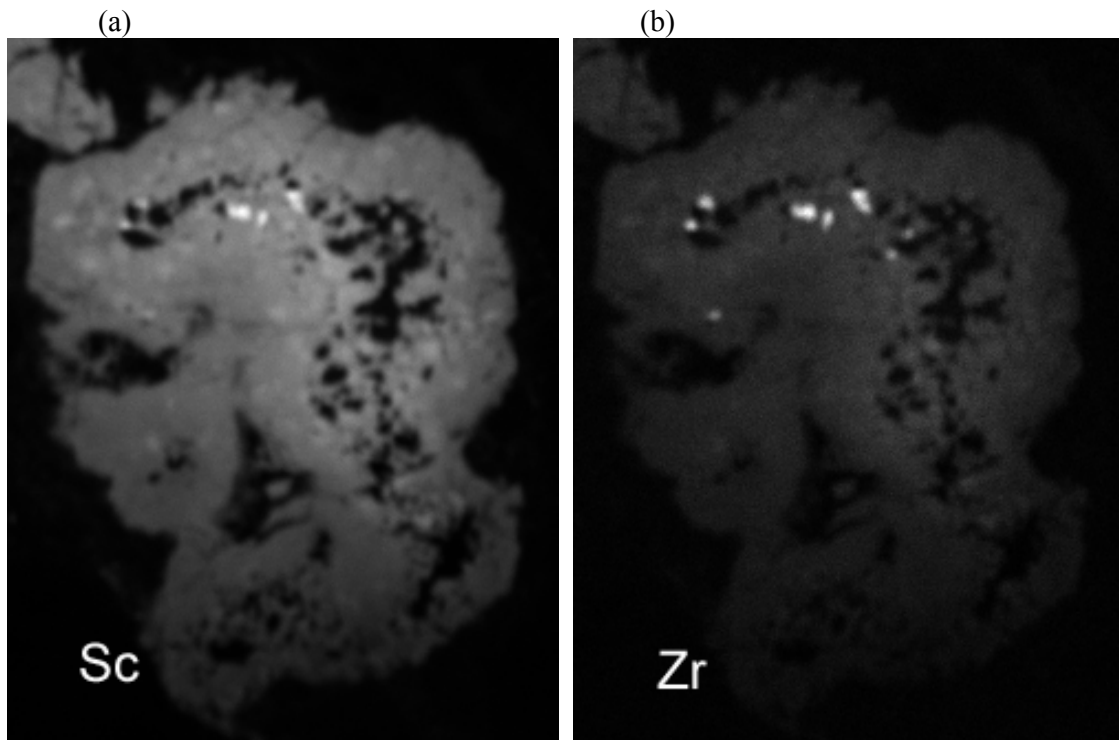
730
731
732



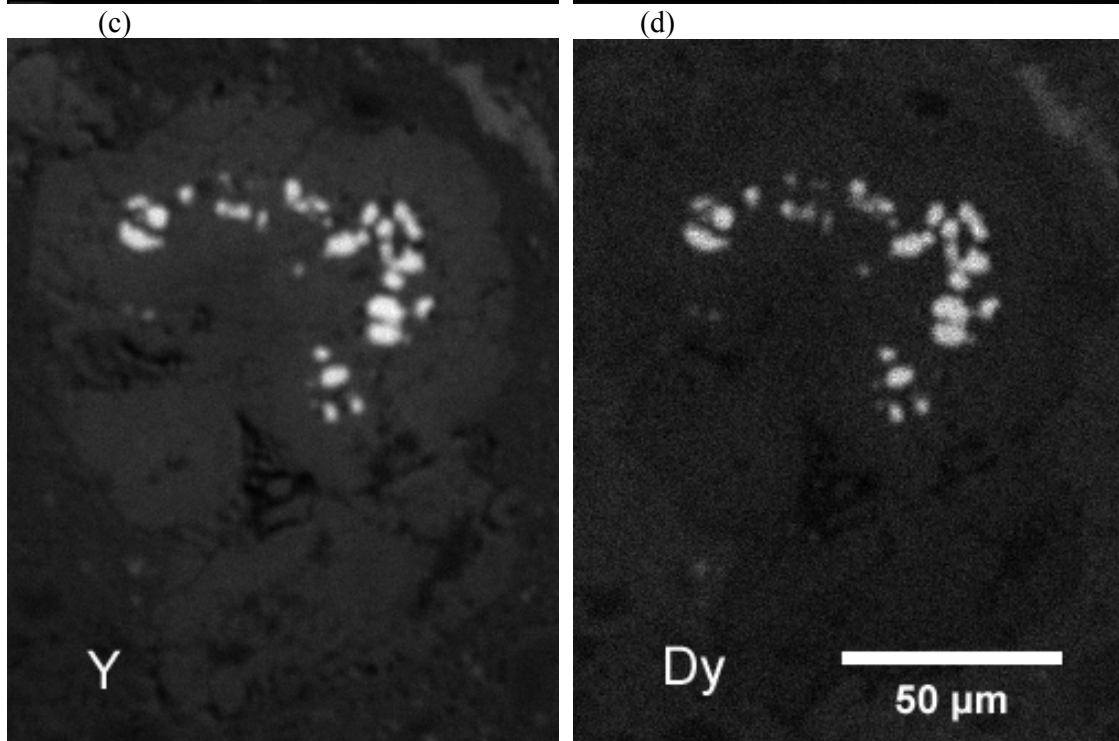
733
734
735
736
737
738
739
740
741

Figure 2. Enlarged BSE images of ACM-3 with contrasts optimized to show kangite microcrystals (type material) with perovskite and spinel in host davisite. The cross mark shown in (a) indicates where the EBSD pattern (shown in Fig. 6) and the synchrotron micro-Laue diffraction data were collected. Scale bar is 1 μm .

742

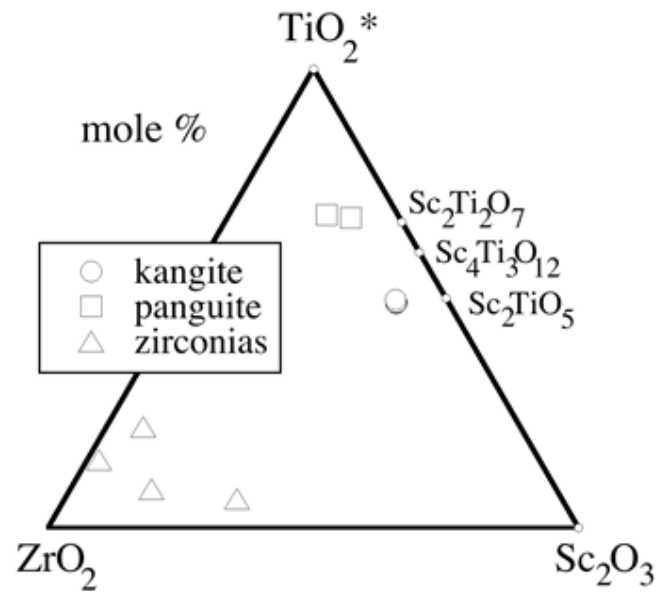


743
744



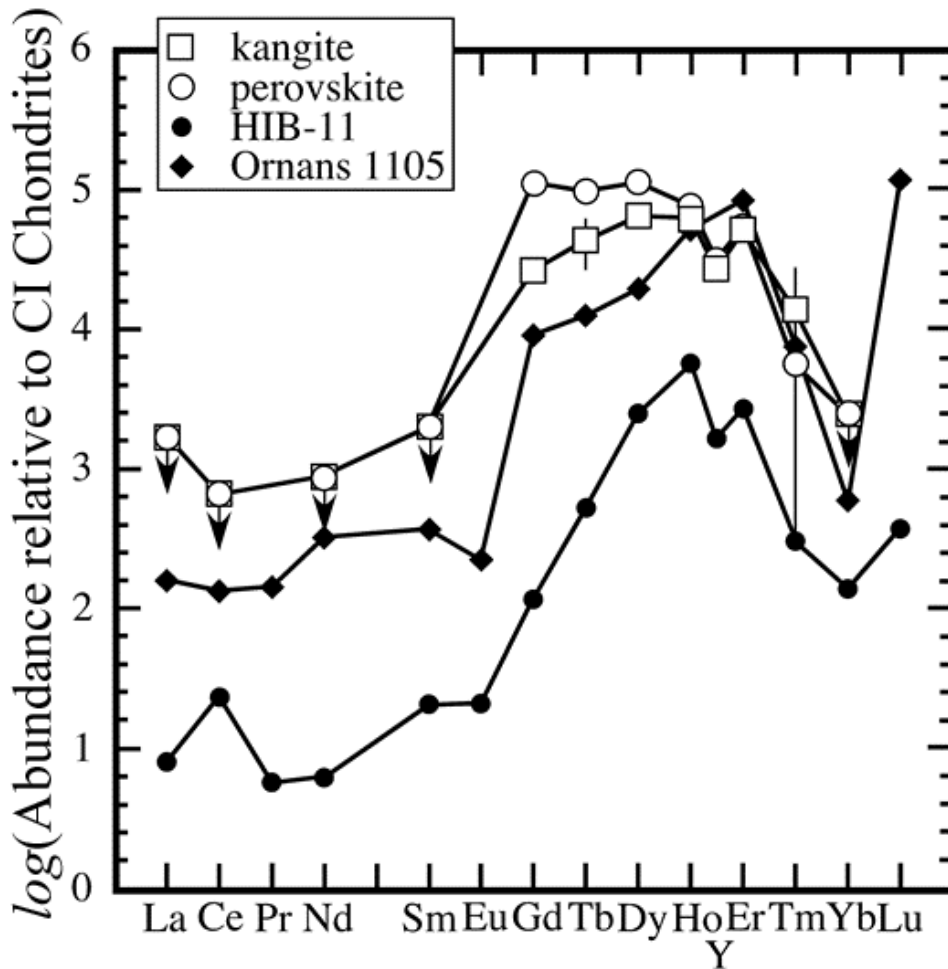
745
746
747
748
749
750
751

Figure 3. Sc, Zr, Y, and Dy X-ray maps of ultrarefractory inclusion ACM-3. Scale bar is 50 μm.



752
753
754
755
756
757
758
759
760
761
762
763
764

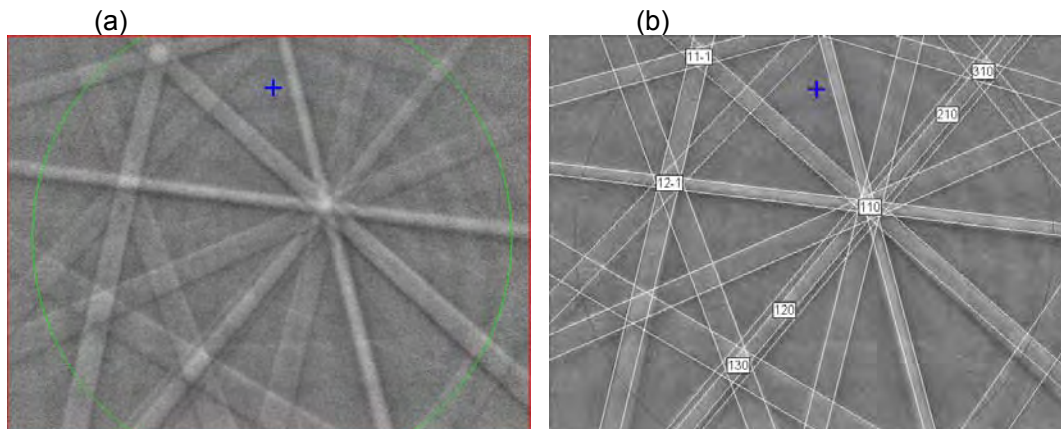
Figure 4. Compositions in mole % of meteoritic Sc-, Zr-enriched oxides in terms of the ternary Sc_2O_3 - TiO_2^* (where all Ti is computed as TiO_2) - ZrO_2 . These three oxides account for 80-97% of cations in the zirconias and 70-74% of the cations in kangite and panguite, the balance being mostly Al, Ca, Mg, and Y. Data are taken from Noonan et al. (1977), Lovering et al. (1979), Hinton et al. (1988), Weber and Bischoff (1994), Ma et al. (2012), and this study.



765
766
767
768
769
770
771
772
773
774
775
776
777
778
779

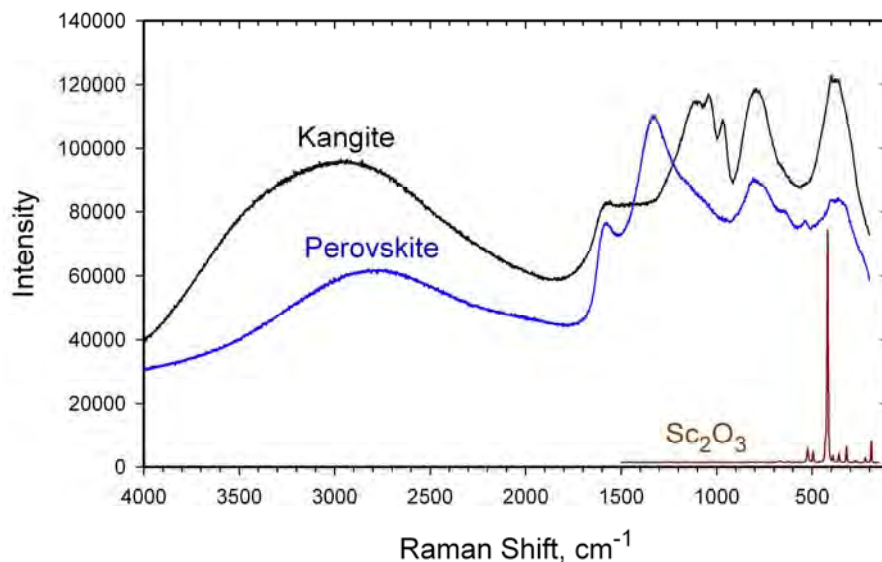
Figure 5. Abundance of REE and Y relative to CI chondrites (Anders and Grevesse 1989) in kangite and perovskite from ACM-3. Error bars for analyses from this study are standard deviations on multiple analyses where larger than the symbols. Downward pointing arrows indicate maximum concentrations set at the detection limit for our EPMA analyses. Also shown are the REE patterns for an ultrarefractory cluster of oxides in Ormans inclusion 1105-42 (Davis 1991) and inclusion HIB-11 from Murchison, which consists of perovskite and spinel in a davisite-rich inclusion (Simon et al. 1996). Error bars for literature analyses are not shown.

780
781
782



783
784
785
786
787
788

Figure 6. (a) EBSD pattern of the kangite crystal marked with a cross in Figure 2a; (b) the same pattern indexed with the cubic $Ia\bar{3}$ structure obtained by synchrotron micro-diffraction.



789
790
791
792
793
794

Figure 7. Raman spectra of kangite and perovskite in ACM-3, and synthetic Sc_2O_3 . The peaks for kangite and perovskite are dominated by optical fluorescence features due to high concentrations of REEs in the crystals so that no Raman shifts can be distinguished.